Supplementary Information (SI) for Energy & Environmental Science.
This journal is © The Royal Society of Chemistry 2025

Supplementary Information

Constructing the built-in electric field across NiMo/NiMoP heterointerface for efficient and durable seawater electrolysis in anion exchange membrane electrolyzers

Yue Xu, Shuaidong Li, Jiawen Cao, Zhongqi Ren, Yingjian He, Zeyun Cai, Chen Hou, Jingzi Zhang, Zuhuang Chen, Rongpei Shi*, Samuel Jeong*, Xi Lin*, Kailong Hu*

Yue Xu, Shuaidong Li, Jiawen Cao, Zhongqi Ren, Yingjian He, Jingzi Zhang, Prof. Zuhuang Chen, Prof. Rongpei Shi, Prof. Xi Lin, Prof. Kailong Hu
School of Materials Science and Engineering, and Institute of Materials Genome & Big Data, Harbin Institute of Technology, Shenzhen 518055, P. R. China
E-mail: hukailong@hit.edu.cn, linxi@hit.edu.cn, shirongpei@hit.edu.cn

Dr. Zeyun Cai
Institute of Special Environments Physical Sciences, Harbin Institute of Technology, Shenzhen 518055, P. R. China.

Dr. J. Zhang
School of Computer Science and Technology, Harbin Institute of Technology, Shenzhen 518055, P. R. China.

Dr. Chen Hou
Shanghai Synchrotron Radiation Facility (SSRF), Shanghai Advanced Research Institute, Chinese Academy of Sciences, 239 Zhangheng Rd, Pudong, shanghai 201203, P. R. China.

Prof. S. Jeong
Institute of Applied Physics, Graduate School of Pure and Applied Sciences,
University of Tsukuba, Tsukuba 305-8573, Japan.
E-mail: jeong.samuel.fp@u.tsukuba.ac.jp

Methods

Preparation of NiMo NWs on Ni foam. The Ni foam (1.0 cm^2, 0.2 cm thickness) was initially subjected to a cleaning process involving acetone, followed by immersion in 1.0 M HNO_3 solution and subsequent rinsing with ultrapure water (resistivity: 18.2 MΩ cm). 1.5 mmol of $NiCl_2·6H_2O$ (99% purity, Macklin Inc.) and 1.5 mmol of $Na_2MoO_4·2H_2O$ (99% purity, Macklin Inc.) were dissolved in 30 mL of ultrapure water. The resulting solution and Ni foams were transferred to a Teflon-coated stainless autoclave being heated at 150 °C for 6 h. After the hydrothermal process, Ni foams were coated by $NiMoO_4$ nanowires (NF@$NiMoO_4$). The NF@$NiMoO_4$ samples were then transferred to a porcelain boat and placed inside a quartz tube. Subsequently, the NiMo alloy NWs coated Ni foam were produced through the heating treatment at 500 °C for 2 h under an atmosphere of Ar (200 sccm) and H_2 (100 sccm).

Preparation of NiMo/NiMoP heterojunctions. The NiMo/NiMoP samples were synthesized via an electrochemical deposition (ECD) process. An Ag/AgCl electrode, a graphite rod, and the NiMo-coated Ni foam were utilized as the reference electrode, counter electrode, and working electrode. The electrolyte was prepared by blending 0.02 mol of $NiCl_2·6H_2O$, 0.015 mol of NaH_2PO_2 (99% purity, Shanghai Aladdin Biochemical Technology Co., Ltd.), 0.004 mol of $Na_2MoO_4·2H_2O$, and 0.03 mol of sodium citrate (99% purity, Hongyan Pte Ltd.) in 100 mL of ultrapure water. The pH value of this electrolyte was adjusted to 6.0 by adding H_2SO_4. The isolated and continuous NiMo/NiMoP heterojunctions (NiMo/NiMoP-I and NiMo/NiMoP-C) were achieved, respectively, under the ECD current of −100 mA for 10 and 20 min.

Preparation of NiMoP sample: The NiMoP samples for LSV tests were synthesized through a direct 20-min ECD process to deposit NiMoP onto Ni foam substrates in the same electrolyte used for NiMo/NiMoP-C synthesis. The NiMoP samples for ultraviolet photoelectron spectroscopy (UPS) tests were synthesized via the same process by substituting carbon cloth (1 cm × 1 cm, Cetech W1S1011) for Ni foam.

Structural characterizations. The microstructure and morphology of the samples were investigated through a scanning electron microscope (SEM, Phenom-Scientific Phenom Pro and Gemini SEM560), transmission electron microscopes (TEM, Hitachi HF5000 and FEI Tecnai G2 F30), and equipped energy disperse spectroscopy (EDS). XRD analysis was performed through the D2 PHASER (Haoyuan Instruments) with Cu Kα1 radiation. Nitrogen adsorption and desorption measurements were performed with a surface area and porosimetry analyzer (Micromeritcs ASAP 2460) at 77.0 K. XPS analysis was conducted by an X-ray photoelectron spectrometer (Thermo Scientific Nexsa) with an Al Kα and X-ray monochromator. The surface potentials were measured by an Asylum Research MFP-3D Infinity atomic force microscope (AFM, Oxford Instruments) with Kelvin probe. AFM samples were prepared through depositing NiMo and NiMoP on a silicon wafer with conductive platinum coating on one side, avoiding the adverse impact of the Ni foam with high surface roughness on the probe. UPS experiments were carried out at the Catalysis and Surface Science station at the BL11U beamline in the National Synchrotron Radiation Laboratory

(NSRL) in Hefei, China. Helium discharge lamps were equipped with He (II) photo line (40 eV). The reflectance data was obtained through Ultraviolet-Visible spectroscopy (UV-Vis Lambda 1050+) on diffuse reflectance mode. The metal concentration in the electrolyte was determined using inductively coupled plasma-mass spectrometry (ICP-MS, NexION 1000).

Measurements of the work function (*Φ*) and valence band maximum (VBM). The energy gap (ΔE) between the fermi level and the VBM was obtained through UPS.[1] The *Φ* values of each sample were calculated by Equation (1):

$$\Phi = 40\ eV - E_{cutoff} \#(1)$$

where E_{cutoff} represents the high-binding energy secondary electron cutoff.

The VBM was obtained by Equation (2):

$$E_{VBM} = 40\ eV - \left(E_{cutoff} - \Delta E\right) \#(2)$$

Determination of the band gap energy (E_g). Reflectance data was measured by UV-Vis for the calculation of E_g. The Kubelka-Munk function was provided for converting reflectance data into scattering and absorption coefficients, typically defined as:[1]

$$F = \frac{(1-R)^2}{2R} = \frac{K}{S} \#(3)$$

where R represents the reflectance of the infinitely thick material, and K and S represent the absorption and scattering coefficients, respectively.

Then given the Tauc plot, the relationship between the absorption coefficient (α) and the photon energy (hv) was expressed as: [2,3]

$$(hv * \alpha)^n = A\left(hv - E_g\right) \#(4)$$

where h represents the Planck constant, v is the frequency of the photon, α is the adsorption index, and A is a constant. The exponent n was set to 2 when dealing with direct transition band gaps. Finally, the E_g energy value was obtained from the x-axis intercept of the linear fit of the Tauc plot. Some important parameters involved in the band structure calculation and BEFs construction are listed in Table S1.

Electrochemical measurements. The electrochemical tests were conducted using a three-electrode system in an electrochemical workstation (BioLogic, VSP-300). An Ag/AgCl electrode, a graphite rod, and as-synthesized samples served as the reference electrode, counter electrode, and working electrode. The neutral simulated seawater was prepared by dissolving 10.74 g of NaCl (99.5% purity, Macklin Inc.), 1.98 g of $MgCl_2 \cdot 6H_2O$ (98% purity, Macklin Inc.), 2.82 g of $MgSO_4 \cdot 7H_2O$ (99% purity, Macklin Inc.), 0.91 g of $CaCl_2 \cdot 6H_2O$ (97% purity, Macklin Inc.), 0.08 g of $NaHCO_3$ (99.8% purity, Macklin Inc.), and 0.28 g of KCl (99.5% purity, Macklin Inc.) in 400 mL of ultrapure water. The electrode potential was automatically *iR*-compensated with 85% of the ohmic resistance. All potential were calibrated with respect to a reversible hydrogen electrode (RHE) using the equation: E(RHE)=E(Ag/AgCl) + 0.0592×pH + 0.197 V. Linear sweep voltammetry (LSV) curves were obtained under a sweep rate of 5 mV s s^{-1}. Electrochemical impedance spectra (EIS) measurements were performed under a frequency ranging from 100 kHz to 100 mHz. The ECSA value was determined by using the equation as following,

$$ECSA = \frac{C_{dl}}{C_s} \times S_{geometric\ area}$$

where C_{dl} is the experimentally obtained capacitance, C_{s} is the specific capacitance (60 μF cm^{-2} was used for the C_{s} of catalysts).[4,5]

AEM electrolyzer cell setup. The PiperION A60 membrane (thickness: 60 μm, Versogen) was pre-soaked in 1 M KOH at room temperature for 2 h. The solution was then replaced with a fresh 1 M KOH solution, and the membrane was soaked again at room temperature for an additional hour to facilitate the conversion from bicarbonate form to hydroxide form, thus optimizing conductivity. After soaking, the membrane was rinsed with ultrapure water until the pH approached 7.0. The AEM electrolyzer was constructed from two Ti plates, four sets of bolts, two gaskets (each with a thickness of 250 μm), and the membrane-electrode assembly (MEA). Two titanium plates were fabricated with a serpentine flow field, featuring a central area of 1.0 cm^2. The MEA was fabricated using a combination of the catalyst-coated substrate and catalyst-coated membrane processes. The NiMo/NiMoP-C catalyst was grown on Ti fiber felt (thickness: 300 μm, area: 1.0 cm^2) producing a catalyst-loaded Ti fiber felt to serve as the cathode diffusion layer. To prepare the IrO_2 ink, 2.0 mg of IrO_2 was uniformly mixed with 350 μL of isopropanol, 50 μL of water, and 2.0 μL of Nafion solution (5 wt%), followed by sonication at room temperature for 1 h. The resulting IrO_2 ink was uniformly spray-coated onto one side of the membrane to achieve a loading of 2.5 mg cm^{-2}. The uncoated Ti fiber felt was utilized as the anode diffusion layer. The membrane was placed between the two Ti fiber felt diffusion layers and hot pressed at 1.0 MPa and 100°C for 2 minutes to obtain a tightly bonded MEA.

Cell testing. A potentiosat (CS2350M, Wuhan Corrtest Instruments Co., Ltd.) was utilized to assess the performance and stability of the AEM electrolyzer. During the testing, the electrolyzer was heated to 60 °C, with a 0.5 M NaCl electrolyte preheated to 70 °C being pumped into the serpentine flow field on the anode side at a flow rate of 6 mL min^{-1} via a peristaltic pump. This setup ensured that the reaction occurred within a stable water circulation at a constant temperature. Subsequently, the I-V polarization curve was obtained at a scan rate of 10 mV s^{-1}, and the stability curve was generated through a CP test at 500 mA cm^{-2} for 350 h at 60 °C. The electrode potential was automatically *iR*-compensated with 85% of the ohmic resistance.

Calculation of the price per gasoline-gallon equivalent (GGE) of H_2. The price per GGE of H_2 was calculated by following equations for instance at a current density of 0.2 A cm^{-2}:

$$H_2 production\ rate@0.2\ A\ cm^{-2} = \frac{0.2\ A\ cm^{-2}}{1.602 \times 10^{-19}\ C \times 2} = 1.036 \times 10^{-6}$$

$$Electrolyzer\ power@0.2\ A\ cm^{-2} = 0.2\ A\ cm^{-2} \times 1.72\ V = 0.344\ W\ cm^{-2}\#(6)$$

$$Price\ per\ GGE\ H_2 = \frac{1\ GGE\ H_2}{H_2 production\ rate \times Electrolyzer\ power \times electricity\ bill}\#(7)$$

where 1 GGE H_2 is 0.997 kg, and electricity bill is $0.02.

DFT calculations. DFT simulations were implemented by using the Vienna ab-initio simulation package (VASP).[6] The exchange-correlation potential was handled through the Perdew-Burke-Ernzerhof (PBE) functional's generalized gradient approximation (GGA).[7] The cutoff energy of plane-wave basis was set to be 400 eV, and the Brillouin zone was sampled with the Monkhorst-Pack 4 × 4 × 1 k-grid. The forces on all atoms were converged to 0.02 eV/Å with the wave functions converged to 10^{-4} eV. To calculate the adsorption energy, the (1 0 0) surfaces of NiMo, NiMoP, and NiMo/NiMoP catalysts were modeled with a vacuum width of 15 Å to avoid periodic interactions along the surface normal. The heterointerface between NiMo and NiMoP was formed by integrating the (1 0 0) surfaces of NiMo and NiMoP. Furthermore, the atoms on both sides of the heterointerface were fixed within two layers during the structural optimization process.

The hydrogen adsorption energy (ΔE_H) was calculated as,

$$\Delta E_H = \frac{1}{n}\left(E_{tot} - E_{sub}\right) - \frac{1}{2}E_{H_2}\#(5)$$

where E_{tot} is the total energy of the substrate with n hydrogen atom adsorbed on the surface, E_{sub} is the total energy of the substrate, and E_{H_2} is the energy of a hydrogen molecule in the gas phase (about −6.7 eV was employed in this work). The Gibbs free energy for the hydrogen absorption was corrected as,

$$\Delta G_H = \Delta E_H + \Delta E_{ZPE} - T\Delta S_H\#(6)$$

where ΔE_{ZPE} represents the difference in zero-point energy between the adsorbed hydrogen and hydrogen in the gas phase, and ΔS_H means the entropy difference between the adsorbed state and the gas phase. As the contribution from the vibrational entropy of H in the adsorbed state was negligibly small, the entropy of hydrogen adsorption was approximately estimated as $\Delta S_H \approx -1/2 S_H$, where S_H represented the entropy of H_2 in the gas phase. The Gibbs free energy with the overall corrections was calculated as $\Delta G_H = \Delta E_H + 0.24$ eV.

Molecular dynamics simulation. Classical molecular dynamics simulations were employed to investigate the surfaces of NiMo and NiMoP in an aqueous environment. The initial NiMo and NiMoP unit cells were obtained from the literatures.[8–10] These unit cells were cleaved along the (0 0 1) plane to generate slabs with a thickness of approximately 5 nm, onto which a layer of NaCl solution, around 10 nm thickness, was subsequently applied. The potential functions used in this study are listed in Table S4. The particle charges for NiMo and NiMoP derived from the first-principle calculations of water molecules on the NiMo and NiMoP surfaces, with CM5 charge models obtained based on charge density distribution.[11] The Lennard-Jones (LJ) parameters for water molecules, Na^+, and Cl^- were consistent with those reported in the literature,[12] while the LJ parameters for the three elements in NiMoP were sourced from the Universal Force Field (UFF).[13] Finally, the density distribution of Cl^- near the interface was analyzed under electric field strengths of 0 V $Å^{-1}$, 0.1 V $Å^{-1}$, and 1.0 V $Å^{-1}$.

Supplementary Figures

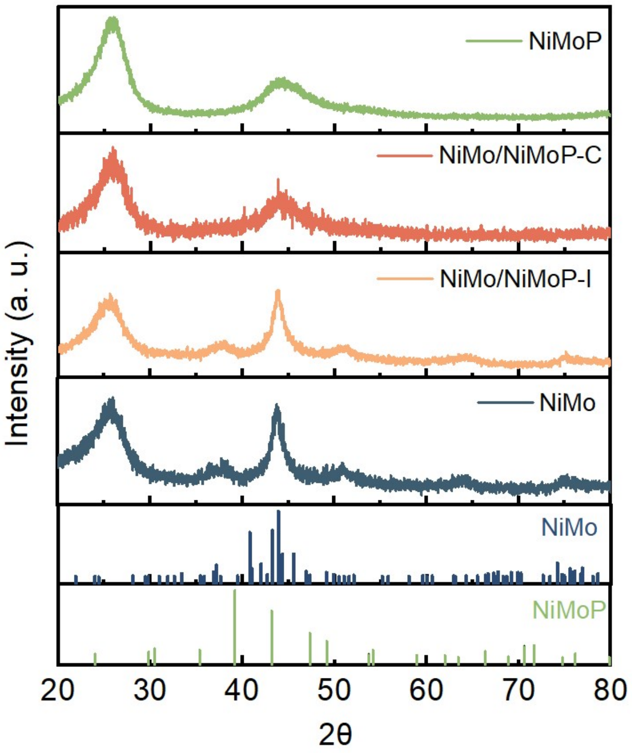

Figure S1. XRD patterns of the NiMoP, NiMo NWs, NiMo/NiMoP-I, and NiMo/NiMoP-C samples.

The samples coated on Ni foam exhibited negligible NiMo peaks, because of the high intensity of Ni foam substrate. Thus, the XRD results of carbon cloth-supported samples are shown to avoid the effect of Ni foam. The broad peaks at approximate 26º and 44º originated from the carbon substrate.

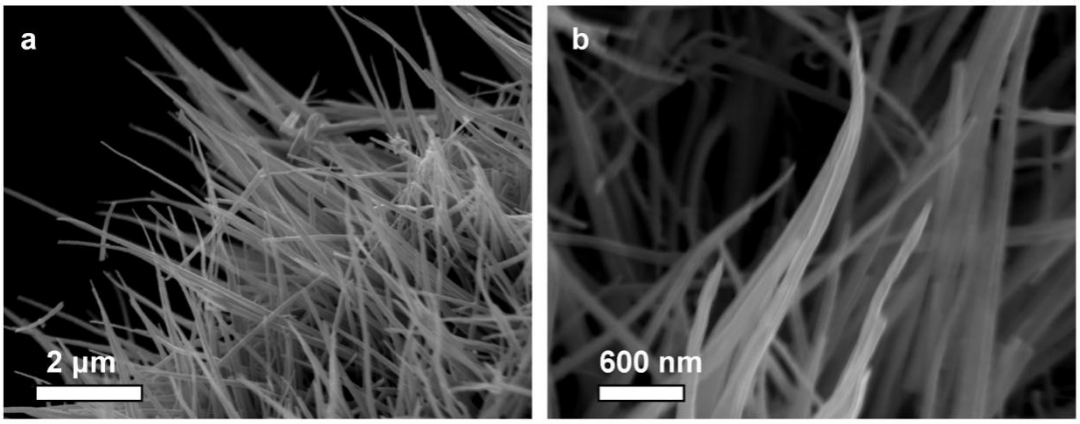

Figure S2. a-b) SEM images of NiMo NWs.

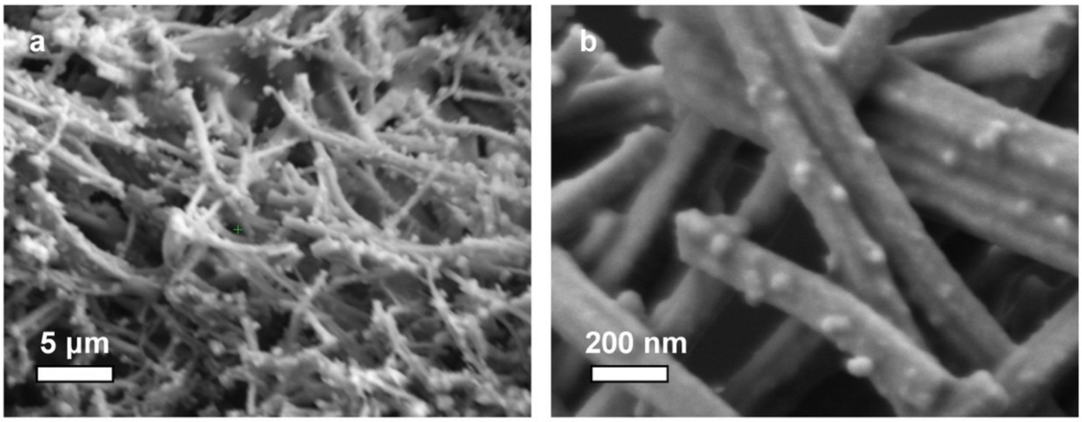

Figure S3. a-b) SEM images of NiMo/NiMoP-I.

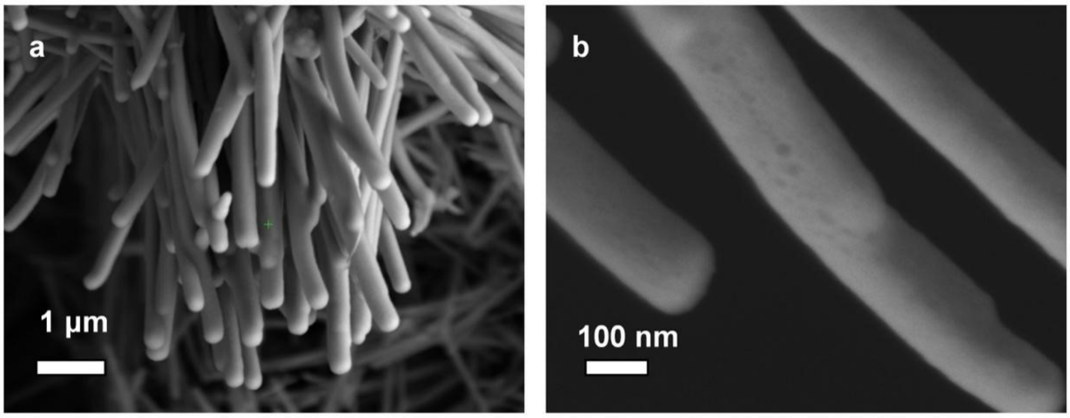

Figure S4. a-b) SEM images of NiMo/NiMoP-C.

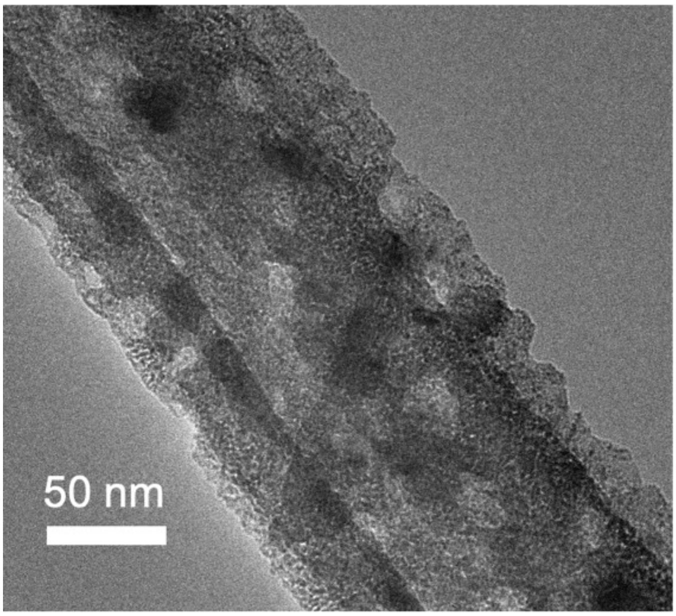

Figure S5. TEM image of NiMo NWs.

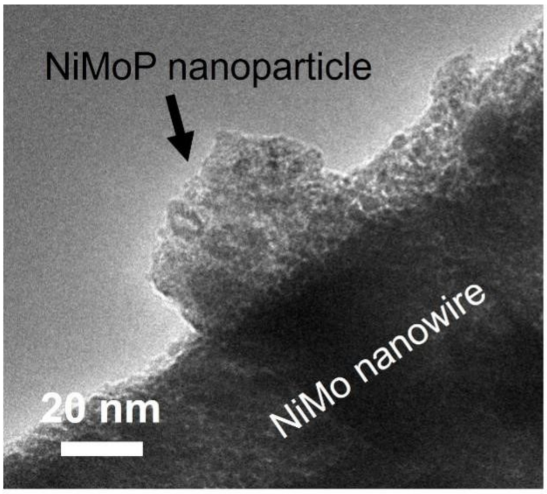

Figure S6. TEM images of NiMo/NiMoP-I.

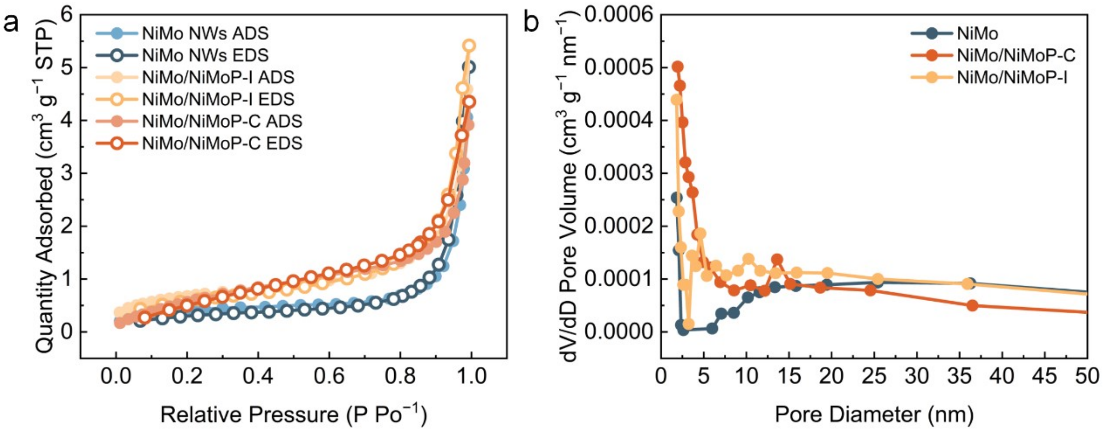

Figure S7. a) Nitrogen adsorption/desorption isotherms and b) pore size distributions of NiMo NWs, NiMo/NiMoP-I, and NiMo/NiMoP-C.

The specific surface area was calculated based on the mass of samples without Ni foam substrate.

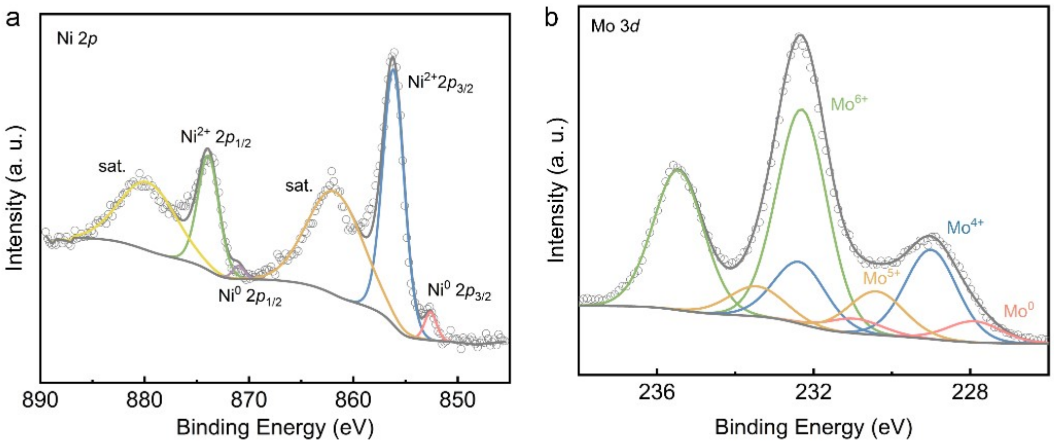

Figure S8. a) Ni 2*p* and b) Mo 3*d* XPS spectra of NiMo NWs.

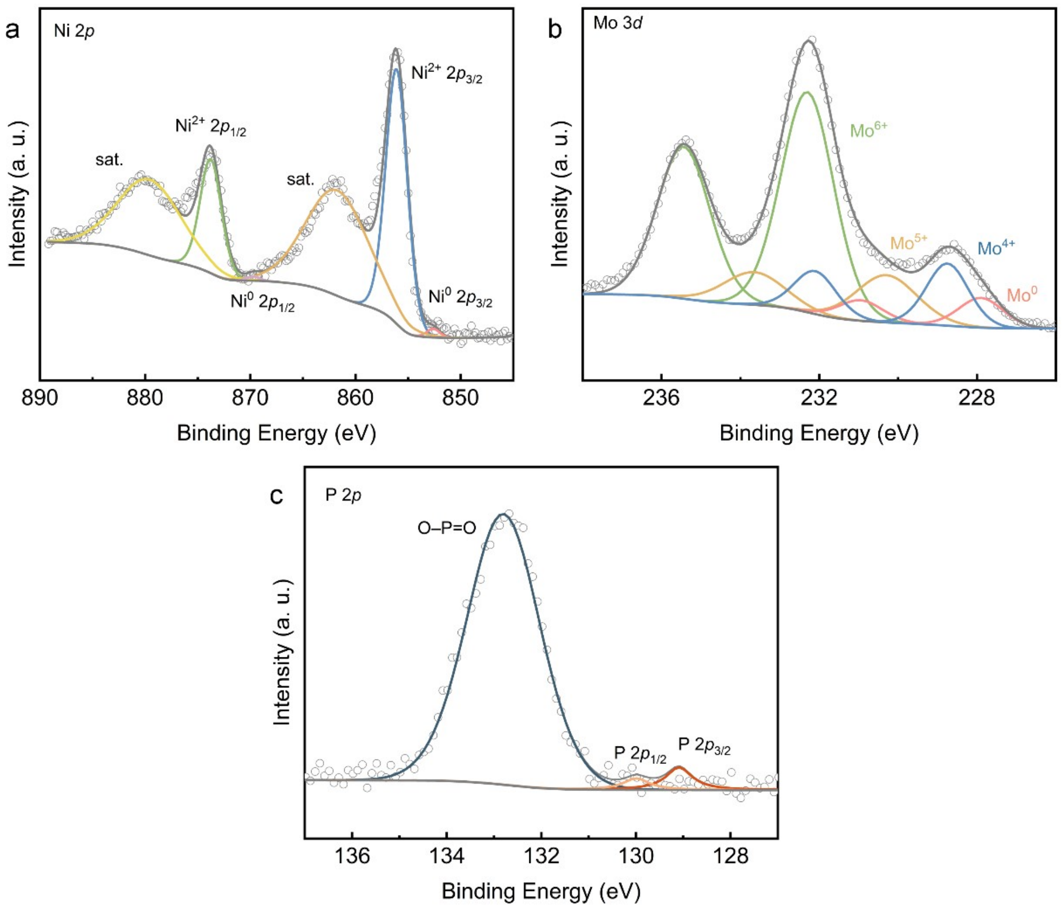

Figure S9. a) Ni 2*p*, b) Mo 3*d*, and c) P 2*p* XPS spectra of NiMo/NiMoP-I.

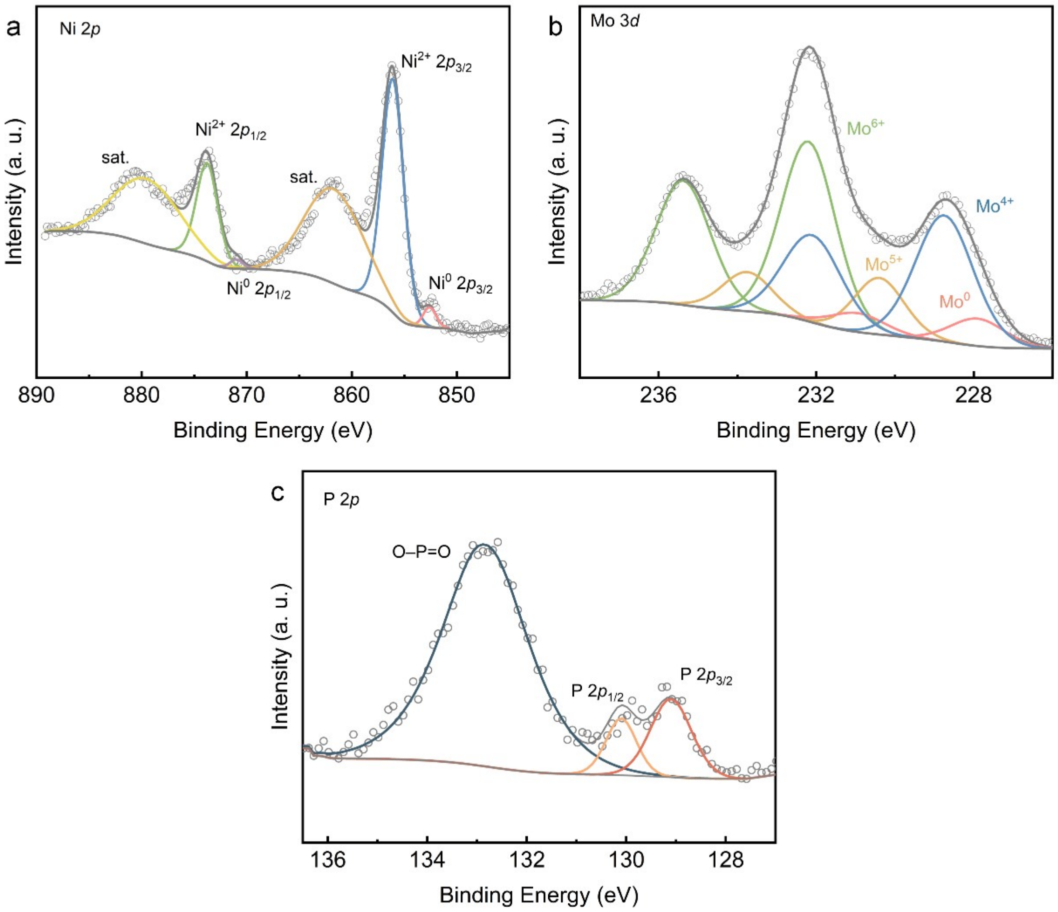

Figure S10. a) Ni 2*p*, b) Mo 3*d*, and c) P 2*p* XPS spectra of NiMo/NiMoP-C.

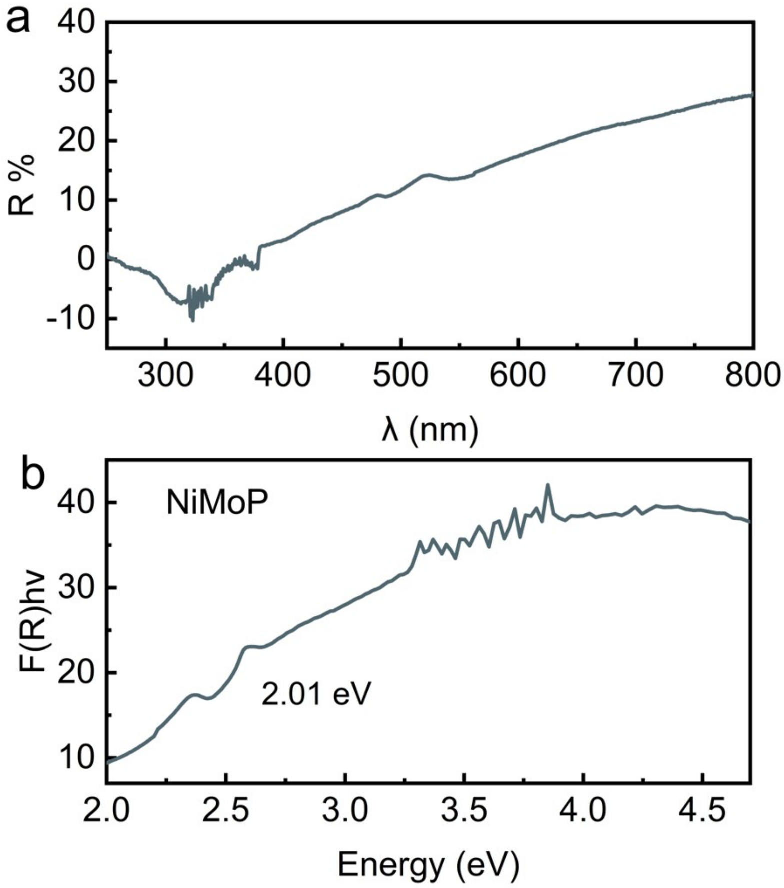

Figure S11. a) UV-vis curve and b) Tauc plot of NiMoP.

The band gap energy values of 2.01 eV were obtained from the x-axis intersection point, which corresponding the steep line drawn from the largest slope region. The calculation details are shown in the methods section.

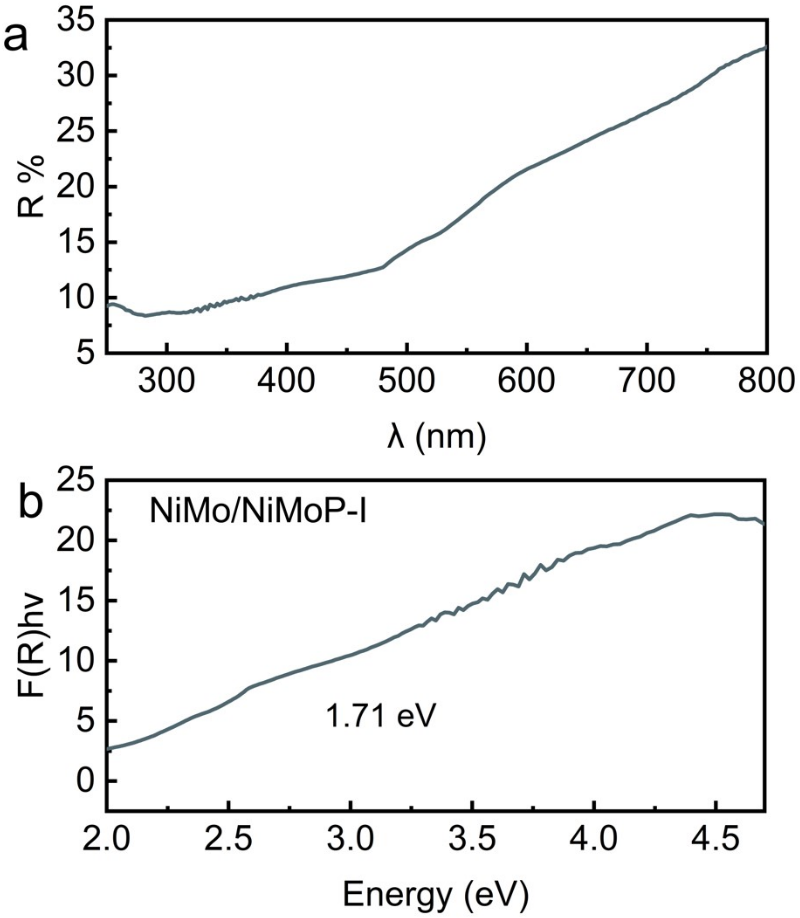

Figure S12. a) UV-vis curve and b) Tauc plot of NiMo/NiMoP-I.

The band gap energy values of 1.71 eV were obtained from the x-axis intersection point, which corresponding the steep line drawn from the largest slope region. The calculation details are shown in the methods section.

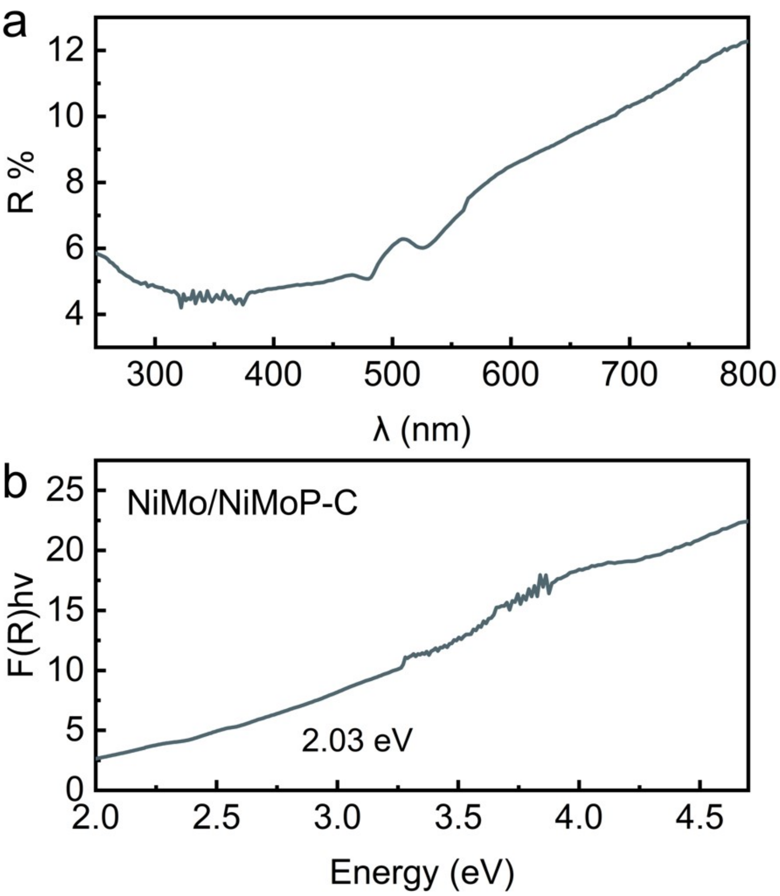

Figure S13. a) UV-vis curve and b) Tauc plot of NiMo/NiMoP-C.

The band gap energy values of 2.03 eV were obtained from the x-axis intersection point, which corresponding the steep line drawn from the largest slope region. The calculation details are shown in the methods section.

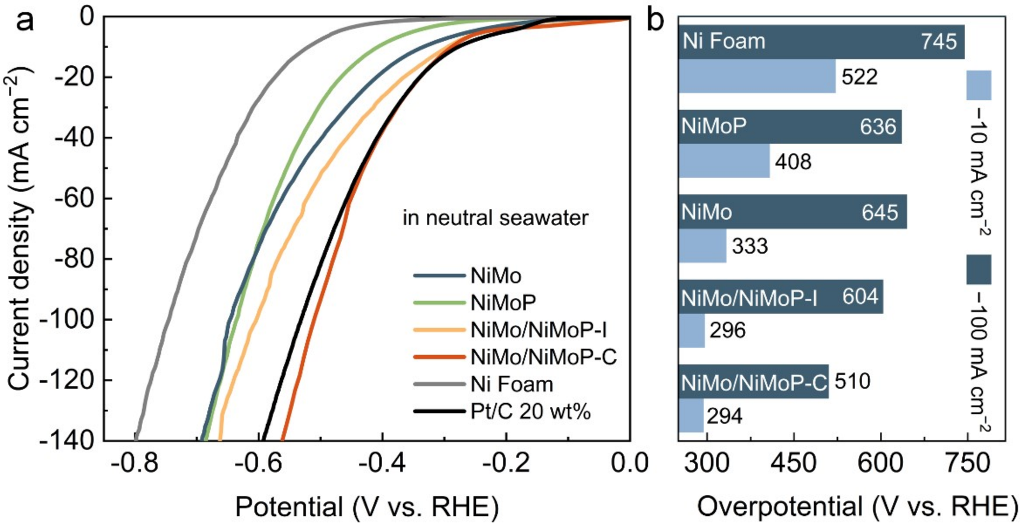

Figure S14. a) HER polarization curves of NiMo, NiMoP, NiMo/NiMoP-I, NiMo/NiMoP-C, Ni Foam, and Pt/C 20 wt% in neutral seawater. b) Comparison of overpotentials at −10 mA cm^{-2} and −100 mA cm^{-2} of NiMo, NiMo/NiMoP-I, and NiMo/NiMoP-C.

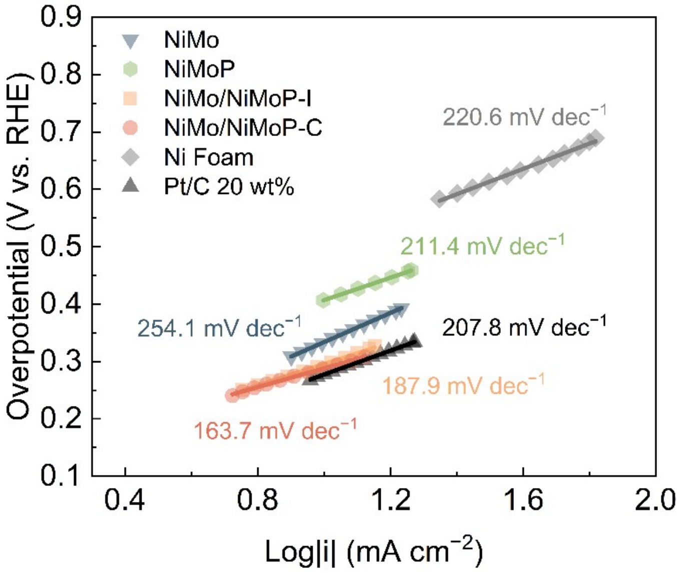

Figure S15. Tafel plots of NiMo, NiMoP, NiMo/NiMoP-I, NiMo/NiMoP-C, Ni Foam, and Pt/C 20 wt%.

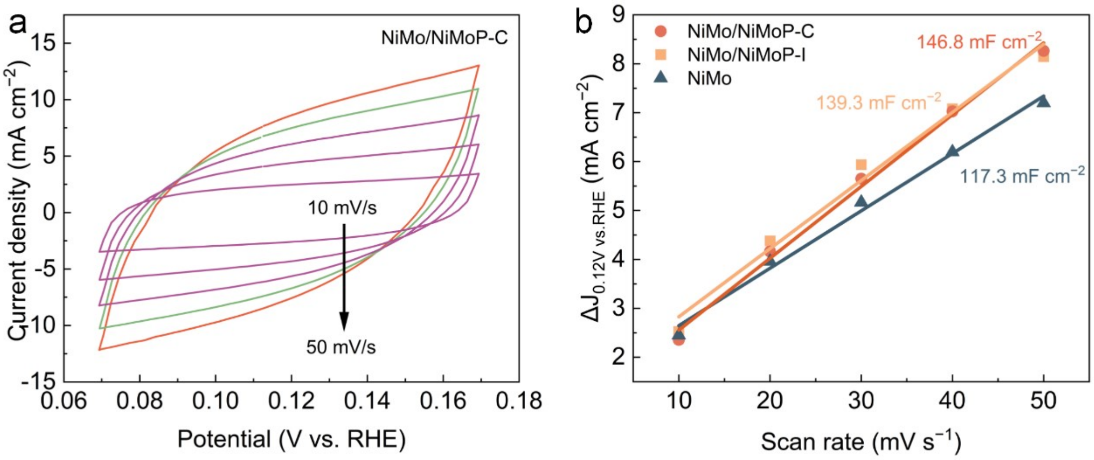

Figure S16. Double layer capacitance measurements. a) Typical CV cycles at different scan rates of NiMo/NiMoP-C. b) Capacitive current density plotted against scan rates for NiMo, NiMo/NiMoP-I, and NiMo/NiMoP-C.

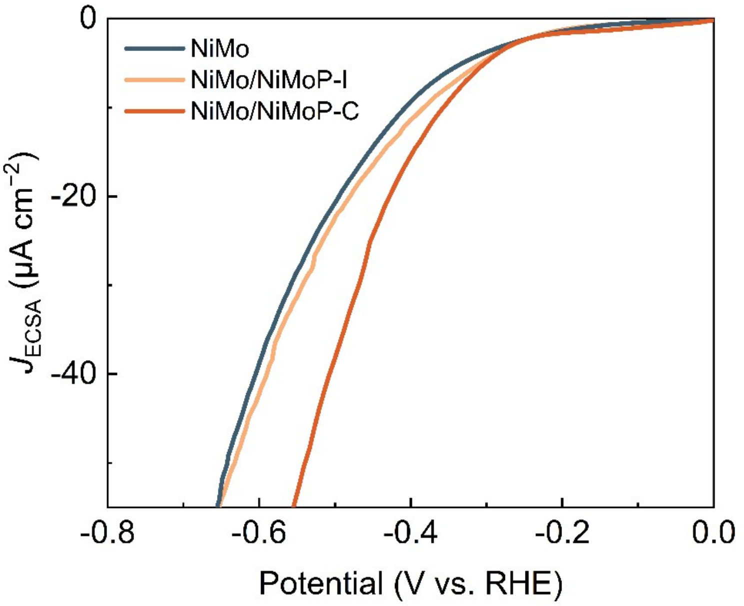

Figure S17. LSV curves of NiMo, NiMo/NiMoP-I, and NiMo/NiMoP-C where the current densities were normalized using the ECSA (J_{ECSA}).

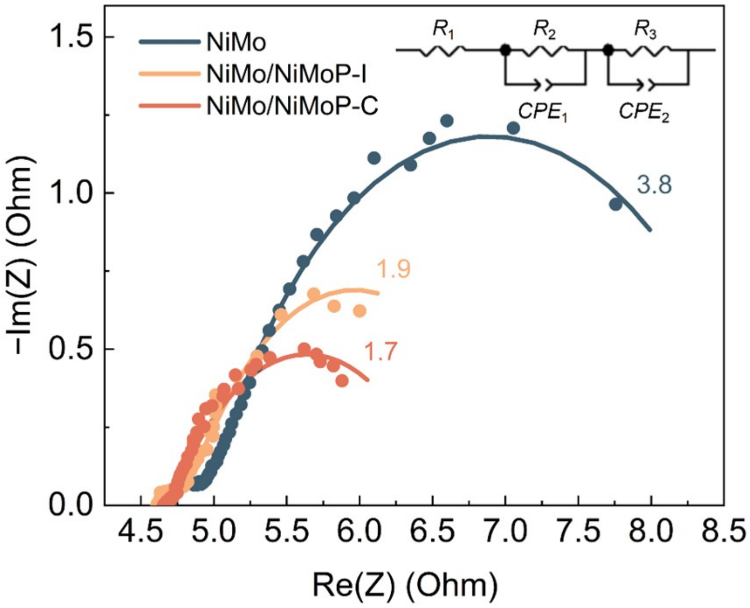

Figure S18. Nyquist plots of each sample. Inset: the corresponding equivalent circuit models. R_1, R_2, and R_3 represent the electrolyte impedance, the electrode surface-related impedance, and the charge-transfer impedance.[14]

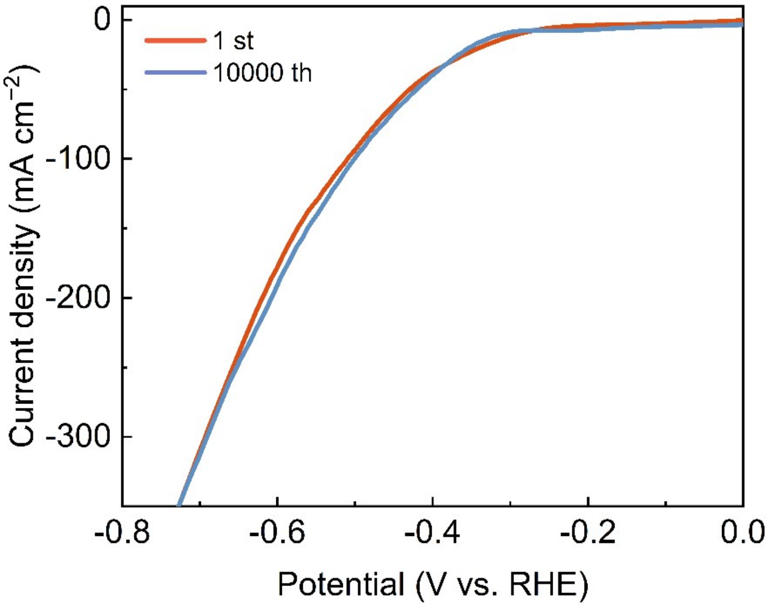

Figure S19. LSV curves of NiMo/NiMoP-C before and after 10000 CV cycles.

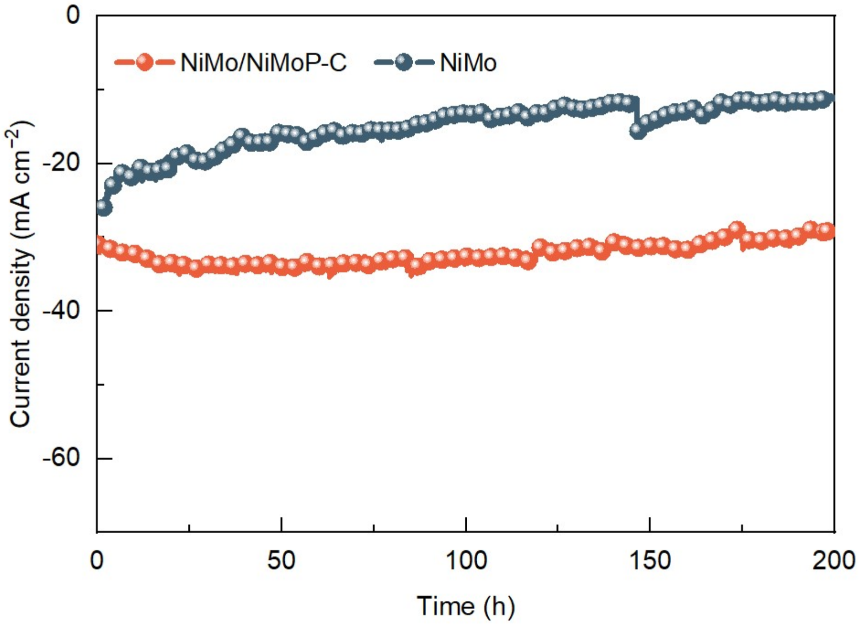

Figure S20. CA test of NiMo and NiMo/NiMoP-C in neutral seawater under the potential of −0.4 V vs. RHE.

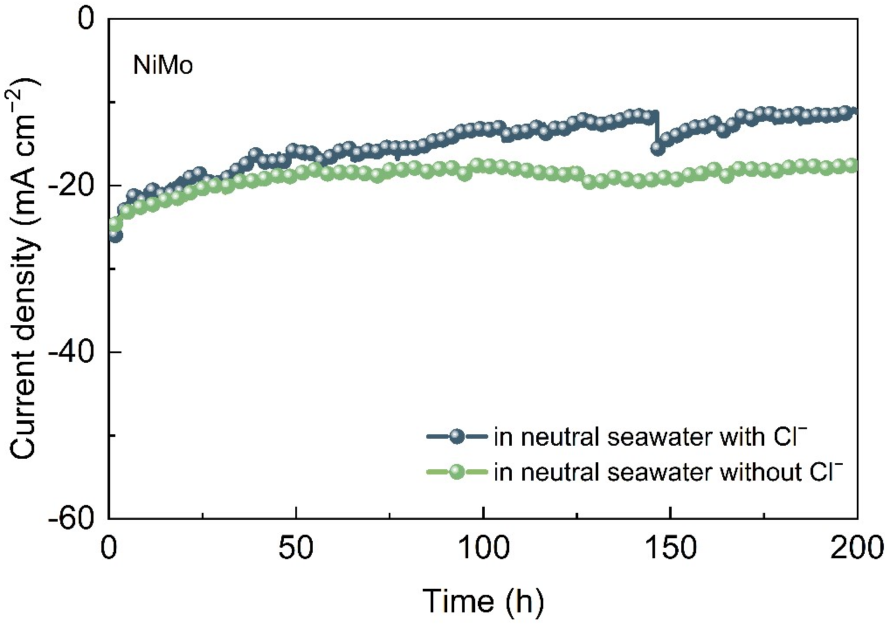

Figure S21. CA tests of NiMo in simulated seawaters with Cl$^-$ and without Cl$^-$ ions under the potential of −0.4 V vs. RHE.

The Cl$^-$-free seawater was prepared by replacing the Cl$^-$ by SO_4^{2-}.

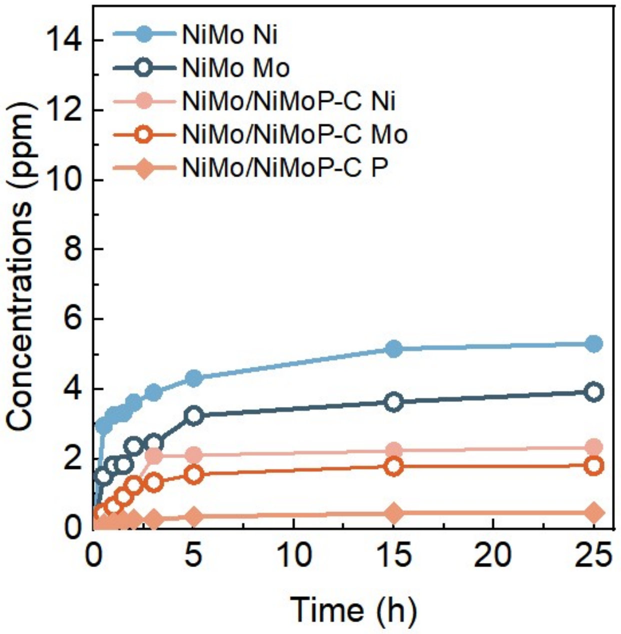

Figure S22. Ni, Mo and P dissolutions of NiMo and NiMo/NiMoP-C during the CA test under the potential of −0.4 V vs. RHE in neutral seawater electrolytes.

The Ni and Mo concentrations in electrolyte were determined through ICP-MS.

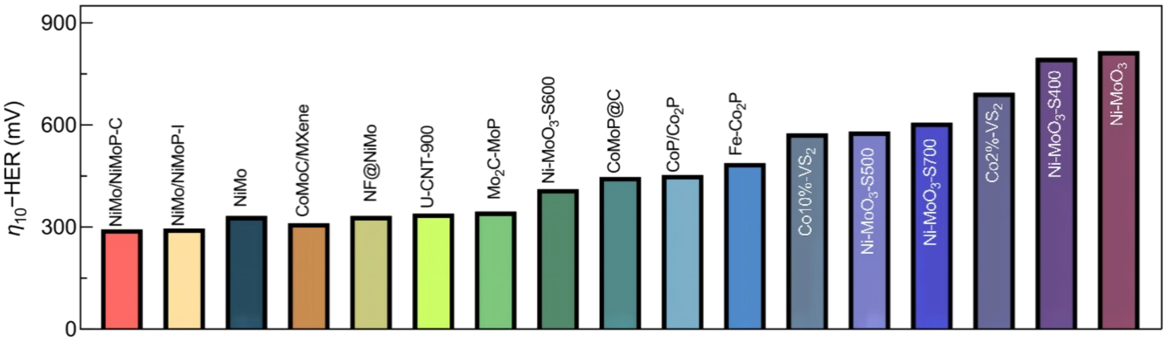

Figure S23. The comparison of HER performances in neutral seawater for samples in this work and other reports.

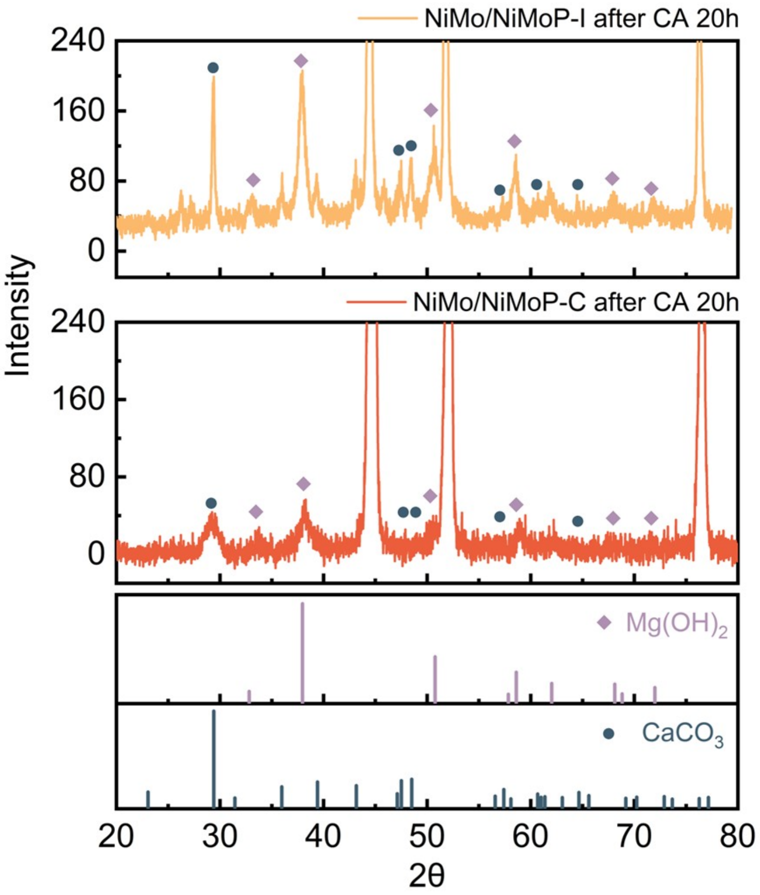

Figure S24. XRD spectra of NiMo/NiMoP-I and NiMo/NiMoP-C after a 200-h HER CA test at a potential of −0.4 V vs. RHE.

The samples coated on Ni foam exhibited negligible NiMo peaks, because of the high intensity of Ni foam substrate. Thus, the XRD results of carbon cloth-supported samples are shown to avoid the effect of Ni foam. The broad peaks at approximate 26º and 44º originated from the carbon substrate.

XRD result suggests that the coated compounds are $Mg(OH)_2$ and $CaCO_3$, which derives from Mg and Ca ions in seawater. During HER process, the pH value of electrolyte gradually increases around the catalyst surface, owing the consumption of protons. This pH variation results in an alkaline microenvironment, and thereby triggers the formation of $Mg(OH)_2$ and $CaCO_3$. Since the test frequency and accumulate time in the XRD tests are identical, the peak intensity can be considered a qualitative indicator of surface precipitate content.

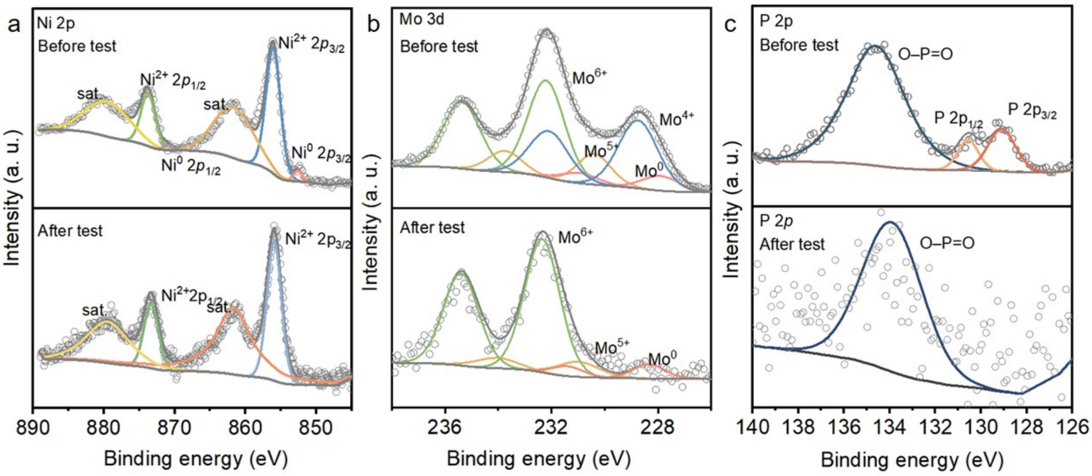

Figure S25. a) XPS Ni 2*p*, b) Mo 3*d* and c) P 2*p* spectra of NiMo/NiMoP-C before and after a 200-h CA test at a potential of −0.4 V vs. RHE.

The disappearance of the Ni^0 peak is attributed to the oxidation during the long-term test. Although some Mo^0 and Mo^{5+} peaks remain, the majority of Mo is oxidized to Mo^{6+} state. P is entirely converted into its oxidized form.

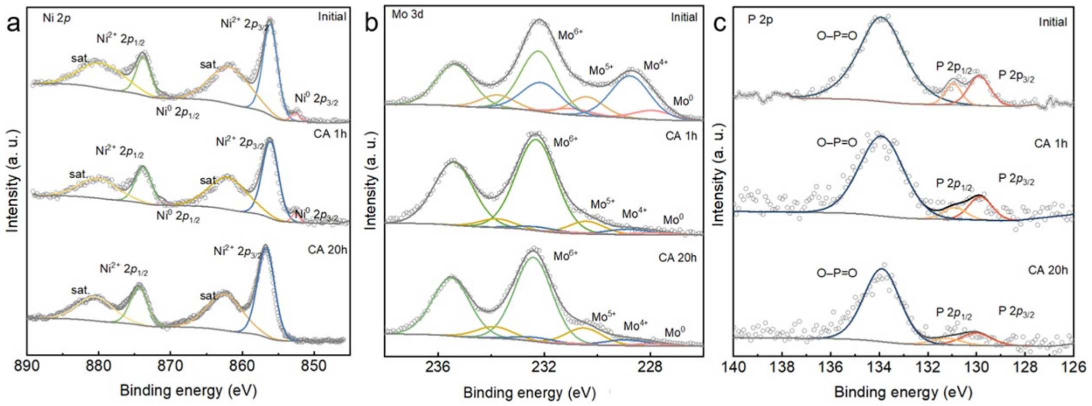

Figure S26. The a) Ni 2*p*, b) Mo 3*d* and c) P 2*p* XPS spectra of NiMo/NiMoP-C before (initial) and after CA tests at a potential of −0.4 V vs. RHE for 1 and 20 h.

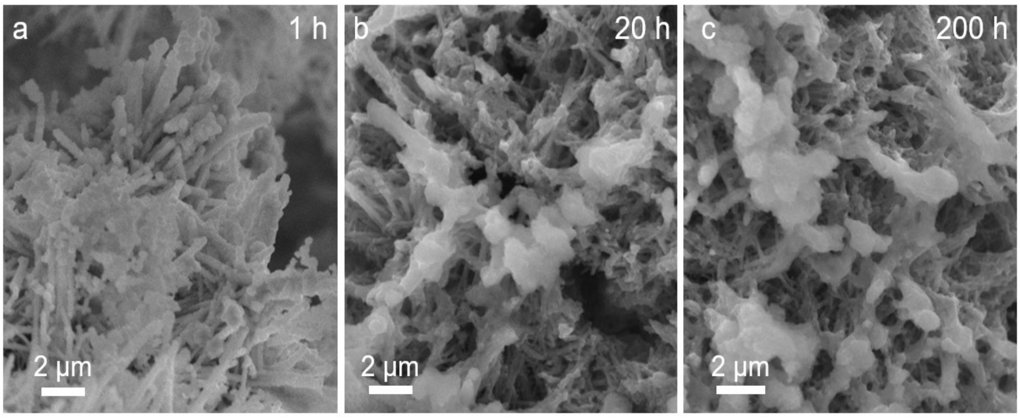

Figure S27. SEM images of NiMo/NiMoP-I after CA tests at a potential of −0.4 V vs. RHE for a) 1, b) 20, and c) 200 h.

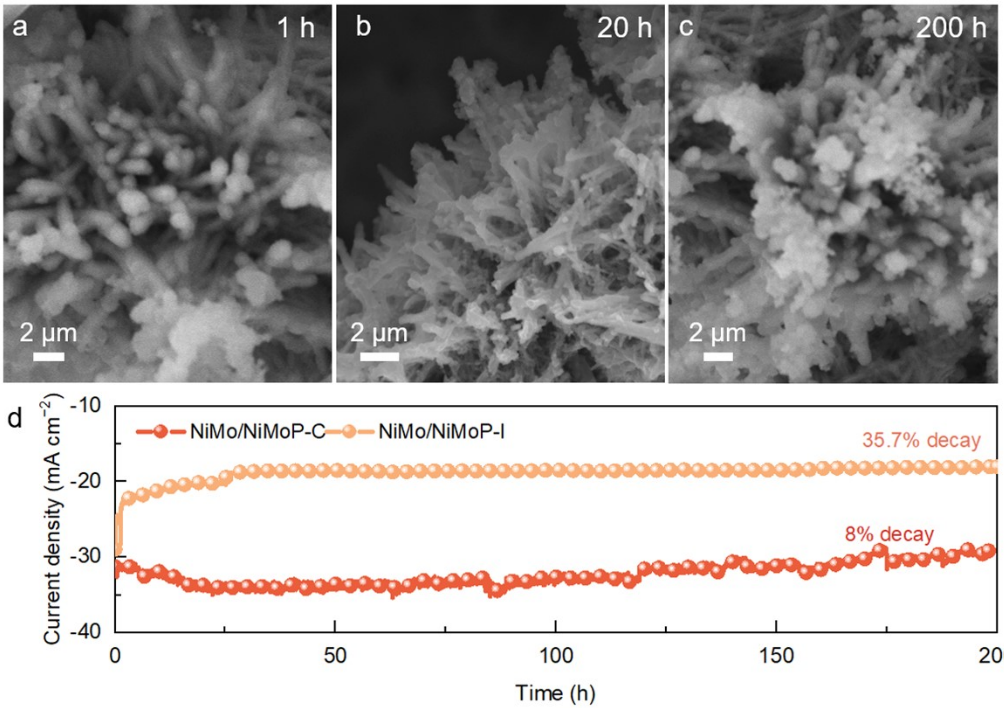

Figure S28. SEM images of NiMo/NiMoP-C after CA tests at a potential of −0.4 V vs. RHE for a) 1, b) 20, and c) 200 h; d) CA curve of NiMo/NiMoP-I and NiMo/NiMoP-C sample under potential of −0.4 V vs. RHE over a 200-h period.

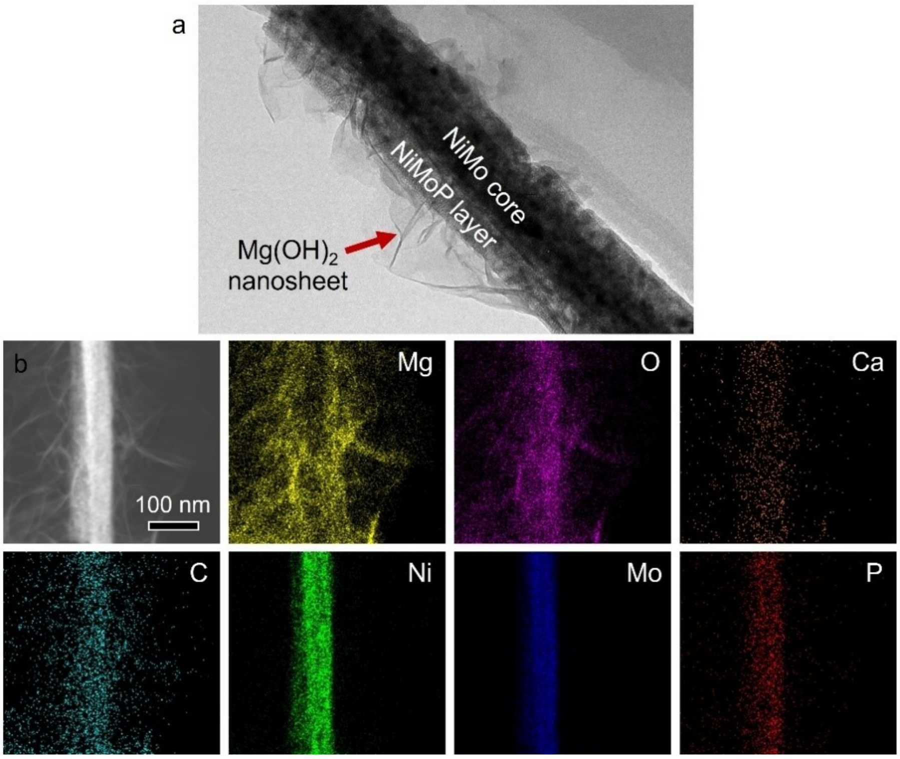

Figure S29. a) TEM image and b) STEM-based EDS elemental mapping of NiMo/NiMoP-C after a 20-h CA test.

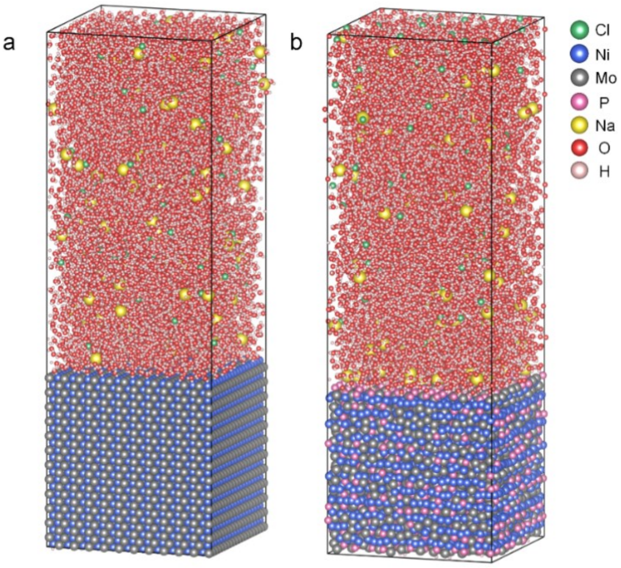

Figure S30. MD models of the electrolyte system of certain ions (Na^+ and Cl^-) in neutral simulated seawater above the surface of a) NiMo and b) NiMoP electrodes without external static electric field applied.

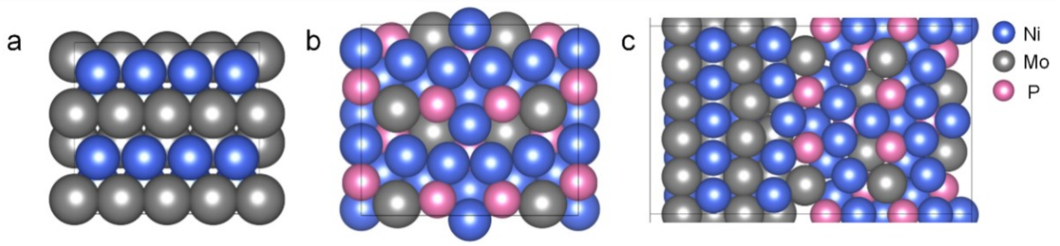

Figure S31. DFT models of a) NiMo surface, b) NiMoP surface, and c) NiMo/NiMoP-C heterointerface.

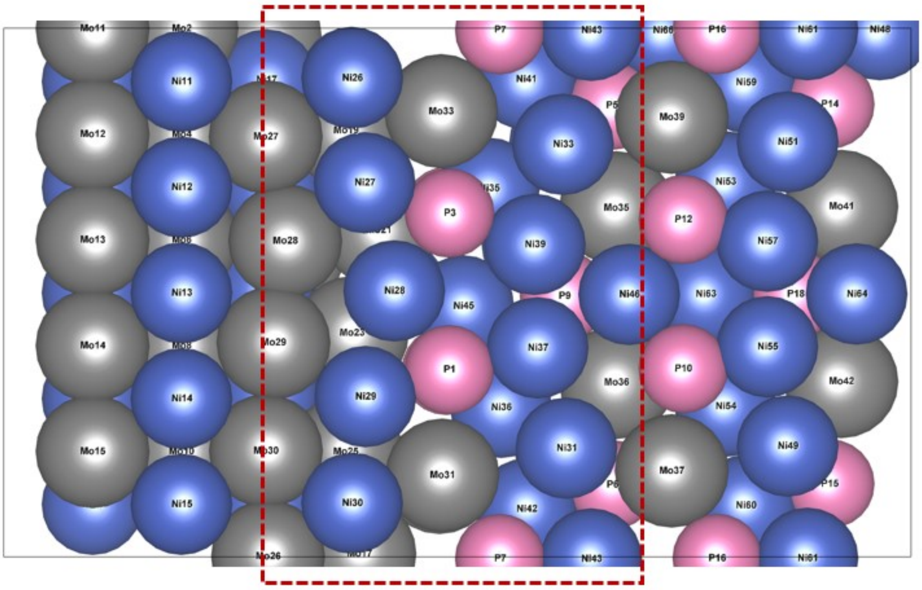

Figure S32. DFT model of the NiMo/NiMoP heterointerface.

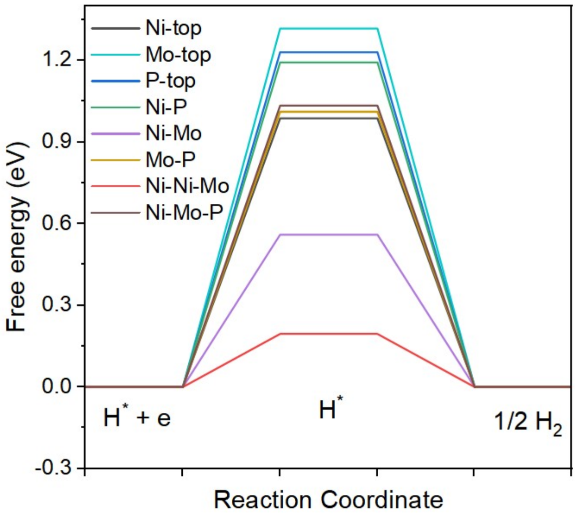

Figure S33. Gibbs free energies of H adsorption on specific sites located at the NiMo/NiMoP interface.

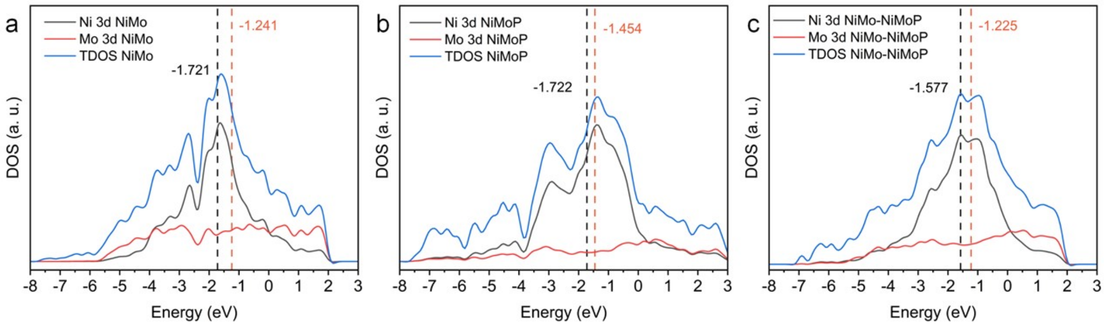

Figure S34. DOS plots of a) NiMo, b) NiMoP, and c) NiMo/NiMoP. The positions of d-band centers are highlighted.

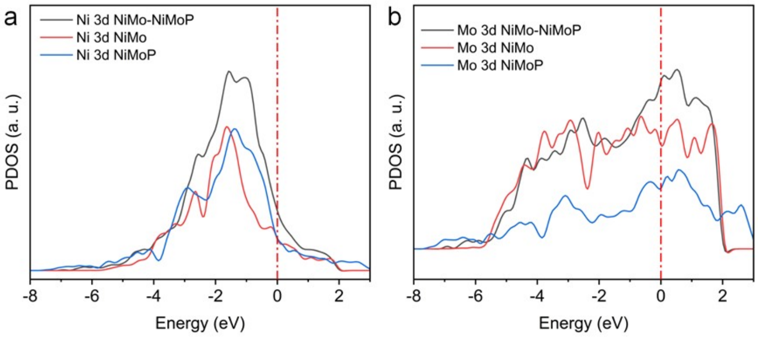

Figure S35. PDOS plots of a) Ni 3*d* and b) Mo 3*d* orbitals in NiMo, NiMoP, and NiMo/NiMoP with highlighted Fermi level.

Table S1. Important parameters involved in the band structure calculation and BEFs construction.

Samples	E_{cutoff} (eV)	ΔE (eV)	Φ (eV)	E_g (eV)
NiMo	35.7	1.10	−4.3	−
NiMoP	36.0	1.24	−4.0	2.01
NiMo/NiMoP-I	36.1	0.50	−3.9	1.71
NiMo/NiMoP-C	36.4	0.95	−3.6	2.03

Table S2. The comparison of HER performances in neutral seawater for samples in this work and other reports.

Catalyst	η_{10}−HER (mV)	η_{100}−HER (mV)	Tafel slope (mV dec^{-1})	Electrolyte	Reference
NF@NiMo	333	645	188.6	Simulated seawater	This work
NiMo/NiMoP-I	296	604	169.9	Simulated seawater	This work
NiMo/NiMoP-C	294	510	163.7	Simulated seawater	This work
Co10%-VS_2	576	−	214	Simulated seawater	15
Co2%-VS_2	696	−	−	Simulated seawater	15
CoP/Co_2P	454	−	107	Simulated seawater	16
Ni-MoO_3-S600	412	−	171	Simulated seawater	17
Ni-MoO_3	818	−	493	Simulated seawater	17
Ni-MoO_3-S400	798	−	478	Simulated seawater	17
Ni-MoO_3-S500	581	−	202	Simulated seawater	17
Ni-MoO_3-S700	608	−	201	Simulated seawater	17
Mo_2C-MoP NPC/CFP	346	−	173	Natural seawater	17
Co/Co_3O_4@C	−	1141	−	Natural seawater	19
U-CNT-900	340	−	−	Natural seawater	20
Co_3Mo_3C/CNT	124	577	249	Natural seawater	21
CoMoC/MXene/NC	312	−	−	Natural seawater	22
Fe-Co_2P	489	−	−	Natural seawater	23
CoMoP@C	448	−	−	Simulated seawater	24

Table S3. The proportion of Ni and Mo valence states of NiMo/NiMoP-C samples before and after a 200-h CA test at the potential of −0.4 V vs. RHE.

Sample	Element	Ratio (at.%)
NiMo/NiMoP-C (Initial state)	Mo^0	6.60
	Mo^{4+}	33.20
	Mo^{5+}	12.80
	Mo^{6+}	47.40
	Ni^0	3.40
	Ni^{2+}	36.40
	Ni sat.	60.20
	P	18.9
	O−P=O	81.1
NiMo/NiMoP-C (After a 200-h CA test)	Mo^0	10.6
	Mo^{4+}	19.2
	Mo^{5+}	9.9
	Mo^{6+}	60.3
	Ni^0	0
	Ni^{2+}	42.57
	Ni sat.	57.43
	P	0
	O−P=O	100

Table S4. Total fitted peak area of samples' surface Mg and Ca characteristic peaks obtained from XPS analysis.

Sample	Area of Mg peak	Area of Ca peak
NiMo/NiMoP-I after a 20-h CA	29081	30166
NiMo/NiMoP-C after a 200-h CA	23658	17969
NiMo/NiMoP-I after a 20-h CA	46690	36476
NiMo/NiMoP-C after a 200-h CA	41524	35267

Table S5. Flow-type electrolyzer performance comparison between the NiMo/NiMoP catalyst and reported highly active catalysts in neutral seawater.

Catalyst	Current density (mA cm^{-2})	Voltage (V)	Current density and stability	Electrolyte	Reference
NiMo/NiMoP-C	1000	1.8	500 mA cm^{-2} 250 h	Simulated seawater 0.5 M NaCl	This work
$Co_{3-x}Pd_xO_4$	1000	1.87	100 mA cm^{-2} 65 h	Natural seawater	24
Ni-$FeWO_4$@WO_3	200	1.6	200 mA cm^{-2} 250 h	Natural seawater	25
Fe,P-$NiSe_2$ NFs	800	1.8	1.8 V; 200 h	Natural seawater	26
Cr_2O_3-CoO_x	1000	1.87	500 mA cm^{-2} 100 h	Natural seawater	4
Ni-Fe-P	400	1.66	500 mA cm^{-2} 100 h	Natural seawater	27

Table S6. The potential functions of Molecular dynamics simulation.

\		ε (kcal mol^{-1})	σ (Å)	q (e)
Na^+		0.352642	2.15954	+1
Cl^-		0.012785	3.22979	−1
H_2O	H	0	0	0.4238
	O	0.15532	3.1662	−0.8476
NiMo	Ni	0.015	2.524806967	0.275
	Mo	0.056	2.719022888	−0.275
NiMoP	Ni	0.015	2.524806967	−0.115152388
	Mo	0.056	2.719022888	0.460616501
	P	0.305	3.694556984	−0.56691745

Table S7. The data of electron gain or loss of each atom in the near-interface region (within the range of the red dashed box) in Figure S32. The positive number represents electron gain, while negative number represents electron loss.

Element	Electron (e)	Element	Electron (e)
Ni16	0.325558	Ni42	0.039357
Ni18	0.252511	Ni45	−0.152521
Ni20	0.002545	Mo19	−0.311771
Ni22	0.291792	Mo21	−0.501725
Ni24	0.345840	Mo23	−0.504314
Ni26	0.280727	Mo25	−0.392602
Ni27	0.200507	Mo31	−0.454458
Ni28	0.002924	Mo32	−0.533175
Ni29	0.248089	Mo33	−0.476230
Ni30	0.290507	Mo34	−0.543000
Ni31	0.047709	Mo35	−1.409000
Ni32	0.043081	Mo36	−1.453400
Ni33	0.017782	Mo37	−1.087100
Ni34	0.014406	Mo39	−1.058000
Ni35	0.042084	P1	−0.572670
Ni36	0.040720	P2	−0.552844
Ni37	−0.031519	P3	−0.476274
Ni38	−0.040714	P4	−0.476932
Ni39	−0.000158	P7	−0.513091
Ni40	−0.007978	P8	−0.509376
Ni41	0.039951	P9	−0.556116

Note: The element numbers not displayed in the figure are due to the viewing angle, which prevents the full visibility of the underlying atoms.

Table S8. The average statistical results of gained or lost electrons by each element at the NiMo/NiMoP interface. The positive number represents electron gain, while negative number represents electron loss.

Sample		Electron (e)	Sample		Electron (e)
NiMo	Ni	0.198	NiMoP	Ni	0.003
	Mo	−0.382		Mo	−0.828
	P	-		P	−0.443

Note: the absolute charge transfer value at the interface is not exactly 0 due to the statistical selection range. The additional charge contribution originates from spontaneous charge transfer among elements from the whole bulk.

Table S9. The DFT calculations results for different adsorption sites on NiMo and the corresponding ΔG_H values.

Adsorption Site	Ni top	Mo top	Ni-Ni bridge	Mo-Mo bridge	Ni-Mo bridge	Mo-Mo-Ni hollow	Ni-Ni-Mo hollow
ΔG_H	−0.49	0.36	−0.34	−0.84	−0.87	−0.45	−0.45

Table S10. The DFT calculations results for different adsorption sites on NiMoP and the corresponding ΔG_H values.

Adsorption Site	Ni top	Mo top	P top	Ni-Mo bridge	Ni-P bridge	Ni-Ni-Mo hollow	Ni-Mo-P hollow
ΔG_H	−0.36	−0.73	−0.34	−0.92	−0.36	−0.33	−0.69

Table S11. The DFT calculations results for different adsorption sites on NiMo/NiMoP interface and the corresponding ΔG_H values.

Adsorption Site	Ni top	Mo top	P top	Ni-Mo bridge	Ni-P bridge	Mo-P bridge	Ni-Mo-P hollow	Ni-Ni-Mo hollow
ΔG_H	0.99	1.32	1.23	0.56	1.19	1.01	1.03	0.19

Note: The selection of adsorption sites in the main text was optimized based on the calculation results of corresponding adsorption energy for different sites as shown in Table S9-11.

References

[1] L. Zhai, X. She, L. Zhuang, Y. Li, R. Ding, X. Guo, Y. Zhang, Y. Zhu, K. Xu, H. J. Fan, S. P. Lau, *Angew. Chem. Int. Ed.* **2022**, *61*, e202116057.

[2] J. Tauc, R. Grigorovici, A. Vancu, *Phys. Status Solidi B* **1966**, *15*, 627.

[3] P. Makuła, M. Pacia, W. Macyk, *J. Phys. Chem. Lett.* **2018**, *9*, 6814.

[4] J. Guo, Y. Zheng, Z. Hu, C. Zheng, J. Mao, K. Du, M. Jaroniec, S.-Z. Qiao, T. Ling, *Nat. Energy* **2023**, *8*, 264.

[5] C. Wei, S. Sun, D. Mandler, X. Wang, S. Z. Qiao, Z. J. Xu, *Chem. Soc. Rev.* **2019**, *48*, 2518.

[6] P. E. Blöchl, *Phys. Rev. B* **1994**, *50*, 17953.

[7] J. P. Perdew, K. Burke, M. Ernzerhof, *Phys. Rev. Lett.* **1996**, *77*, 3865.

[8] J. E. Saal, S. Kirklin, M. Aykol, B. Meredig, C. Wolverton, *JOM* **2013**, *65*, 1501.

[9] S. Kirklin, J. E. Saal, B. Meredig, A. Thompson, J. W. Doak, M. Aykol, S. Rühl, C. Wolverton, *Npj Comput. Mater.* **2015**, *1*, 1.

[10] Q.-J. Hong, S. V. Ushakov, A. van de Walle, A. Navrotsky, *Proc. Natl. Acad. Sci.* **2022**, *119*, e2209630119.

[11] J. Z. Vilseck, J. Tirado-Rives, W. L. Jorgensen, *J. Chem. Theory Comput.* **2014**, *10*, 2802.

[12] X. Xu, Y. Lu, J. Shi, X. Hao, Z. Ma, K. Yang, T. Zhang, C. Li, D. Zhang, X. Huang, Y. He, *Nat. Commun.* **2023**, *14*, 7708.

[13] A. K. Rappe, C. J. Casewit, K. S. Colwell, W. A. I. Goddard, W. M. Skiff, *J. Am. Chem. Soc.* **1992**, *114*, 10024.

[14] M. Jafarian, O. Azizi, F. Gobal, M. G. Mahjani, *Int. J. Hydrog. Energy* **2007**, *32*, 1686.

[15] M. Zhao, M. Yang, W. Huang, W. Liao, H. Bian, D. Chen, L. Wang, J. Tang, C. Liu, *ChemCatChem* **2021**, *13*, 2138.

[16] G. Liu, M. Wang, Y. Xu, X. Wang, X. Li, J. Liu, X. Cui, L. Jiang, *J. Power Sources* **2021**, *486*, 229351.

[17] T. Yang, Y. Xu, H. Lv, M. Wang, X. Cui, G. Liu, L. Jiang, *ACS Sustain. Chem. Eng.* **2021**, *9*, 13106.

[18] Q. Zhang, X. Zhao, X. Miao, W. Yang, C. Wang, Q. Pan, *Int. J. Hydrog. Energy* **2020**, *45*, 33028.

[19] S. Gao, G.-D. Li, Y. Liu, H. Chen, L.-L. Feng, Y. Wang, M. Yang, D. Wang, S. Wang, X. Zou, *Nanoscale* **2015**, *7*, 2306.

[20] Y. Zhao, Q. Tang, B. He, P. Yang, *RSC Adv.* **2016**, *6*, 93267.

[21] X. Wu, S. Zhou, Z. Wang, J. Liu, W. Pei, P. Yang, J. Zhao, J. Qiu, *Adv. Energy Mater.* **2019**, *9*, 1901333.

[22] Y. Lin, K. Sun, X. Chen, C. Chen, Y. Pan, X. Li, J. Zhang, *J. Energy Chem.* **2021**, *55*, 92.

[23] Y.-Y. Ma, C.-X. Wu, X.-J. Feng, H.-Q. Tan, L.-K. Yan, Y. Liu, Z.-H. Kang, E.-B. Wang, Y.-G. Li, *Energy Environ. Sci.* **2017**, *10*, 788.

[24] N. Wang, P. Ou, S.-F. Hung, J. E. Huang, A. Ozden, J. Abed, I. Grigioni, C. Chen, R.

K. Miao, Y. Yan, J. Zhang, Z. Wang, R. Dorakhan, A. Badreldin, A. Abdel-Wahab, D. Sinton, Y. Liu, H. Liang, E. H. Sargent, *Adv. Mater.* **2023**, *35*, 2210057.

[25] S. Zhao, Y. Wang, Y. Hao, L. Yin, C.-H. Kuo, H.-Y. Chen, L. Li, S. Peng, *Adv. Mater.* **2024**, *36*, 2308925.

[26] J. Chang, G. Wang, Z. Yang, B. Li, Q. Wang, R. Kuliiev, N. Orlovskaya, M. Gu, Y. Du, G. Wang, Y. Yang, *Adv. Mater.* **2021**, *33*, 2101425.

[27] H. Shi, T. Wang, J. Liu, W. Chen, S. Li, J. Liang, S. Liu, X. Liu, Z. Cai, C. Wang, D. Su, Y. Huang, L. Elbaz, Q. Li, *Nat. Commun.* **2023**, *14*, 3934.